The Journal of Chemical Physics

RESEARCH ARTICLE | AUGUST 14 2025

The molecular phase diagram of carbon dioxide by molecular simulations of the TraPPE model FREE

D. González-Salgado ; M. M. Piñeiro ; C. Vega

Check for updates

J. Chem. Phys. 163, 064504 (2025)
https://doi.org/10.1063/5.0281079

View Online Export Citation

Articles You May Be Interested In

Fluid-solid equilibrium of carbon dioxide as obtained from computer simulations of several popular potential models: The role of the quadrupole

J. Chem. Phys. (February 2013)

The role of intermolecular interactions in the prediction of the phase equilibria of carbon dioxide hydrates

J. Chem. Phys. (September 2015)

Thermal conductivity of carbon dioxide from non-equilibrium molecular dynamics: A systematic study of several common force fields

J. Chem. Phys. (October 2014)

25 August 2025 09:47:05

Webinar From Noise to Knowledge
May 13th – Register now
Zurich Instruments
Universität Konstanz

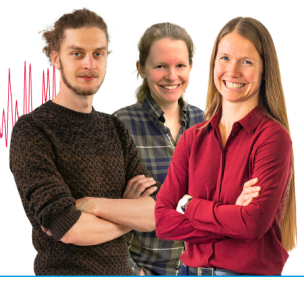

AIP Publishing

The Journal of Chemical Physics ARTICLE pubs.aip.org/aip/jcp

The molecular phase diagram of carbon dioxide by molecular simulations of the TraPPE model

Cite as: J. Chem. Phys. 163, 064504 (2025); doi: 10.1063/5.0281079
Submitted: 16 May 2025 • Accepted: 24 July 2025 •
Published Online: 14 August 2025

View Online Export Citation CrossMark

D. González-Salgado,[1,a)] M. M. Piñeiro,[2] and C. Vega[3]

AFFILIATIONS

[1] Departamento de Física Aplicada, Instituto de Física y Ciencias del Espacio, Universidad de Vigo, As Lagoas s/n 32004 Ourense, Spain
[2] Departamento de Física Aplicada, Universidad de Vigo, 36310 Vigo, Spain
[3] Departamento de Química Física, Facultad de Ciencias Químicas, Universidad Complutense, 28040 Madrid, Spain

[a)] **Author to whom correspondence should be addressed:** dgs@uvigo.gal

ABSTRACT

The determination of the phase diagram of carbon dioxide by using exclusively experimental techniques has been prevented by the strong metastabilities of solid phases and the hysteresis in some phase transitions. Quantum mechanical methods have played a crucial role in this field helping the characterization of the molecular/non molecular character of the phases. Nowadays, it is well-established that CO_2-I, CO_2-II, CO_2-III (first termed as VII), and CO_2-IV phases are molecular phases in contrast with high temperature and high pressure non-molecular phases such as CO_2-V and CO_2-VI. In this work, we explore the ability of the molecular force field TraPPE to describe the molecular part of the carbon dioxide phase diagram by using classical Monte Carlo and molecular dynamics simulations. As it will be shown, this model predicts very accurately the fluid-I transition line and the stability of phases CO_2-I, CO_2-II, CO_2-III, and CO_2-IV in well-defined regions of the phase diagram. The main shortcomings are the small size of the stability regions of CO_2-II and CO_2-III and the appearance of CO_2-II, CO_2-III, and CO_2-IV phases at too low pressures. In addition, the densities of the solid phases are only well-predicted for CO_2-I and at pressures lower than 3 GPa. At higher pressures, the density is underestimated for all the solids. The results clearly indicate that although the TraPPE model does a reasonable job in describing the phase diagram of CO_2, there is still room for improvement.

Published under an exclusive license by AIP Publishing. https://doi.org/10.1063/5.0281079

25 August 2025 09:47:05

I. INTRODUCTION

Increasing concentration of carbon dioxide (CO_2) in the atmosphere and its relation with climate change has had an enormous impact on the scientific and industrial fields, which has provoked great interest in the CO_2 capture technologies.[1] In a more fundamental branch, a vast body of work has been performed to characterize the solid phases and the phase diagram of carbon dioxide, especially in the past decades.[2–51] Under ambient conditions, CO_2 is a gas that transforms in liquid at 6.5 MPa[52] and in solid CO_2-I above 0.5 GPa under isothermal compression.[2,5] This low pressure solid phase is known as "dry ice" and it has a variety of industrial uses especially in food preservation applications. Its crystallographic structure [see Fig. 1(a)] is characterized by fcc cubic lattice (space group *Pa*3) with four molecules per unit cell pointing in the body diagonals directions.[3] This structure, also observed in nitrogen N_2 and carbon monoxide CO, is stabilized by weak quadrupole–quadrupole interactions and presents a low bulk modulus typical from molecular solids. The stability region of this phase comprises the low temperature and pressure region of the T–p phase diagram, as it is shown in Fig. 2. At pressures around 12 GPa (at ambient temperature), the CO_2-I solid transits into the so-called CO_2-III solid phase[10] whose crystallographic characterization as well as its stability domain has been only settled in the past years (it will be discussed in the following). An important feature of this solid in the nineties is that it has served as a starting point to uncover new solid phases. Thus, in 1999, Yoo *et al.*[12] obtained by laser-heating the CO_2-III phase up to 1800 K, a non-molecular tetracoordinated and extended solid phase termed as CO_2-V with extremely high bulk modulus in the range of super-hard materials. The structure determination of CO_2-V has been somewhat controversial and although first was considered as orthorombic $P2_12_12_1$,[12] it was recently claimed that it is a fully tetrahedral partially collapsed variant of SiO_2-β-cristobalite structure of the $I\bar{4}2d$ space group.[38] Its

Published under an exclusive license by AIP Publishing

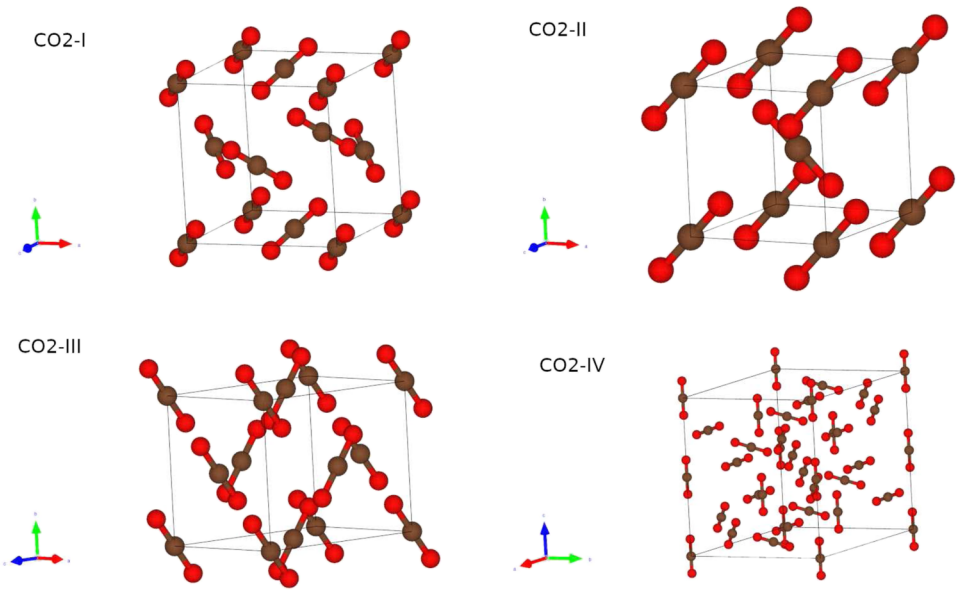

FIG. 1. Unit cells of the molecular phases of carbon dioxide. CO_2-I (cubic, Pa3), CO_2-II (tetragonal, $P4_2/mnm$), CO_2-III (orthorombic, *Cmca*), and CO_2-IV (rhombohedral, $R\bar{3}c$).

stability domain shown in Fig. 2 comprises the high temperature and pressure values of the $p-T$ plane. In 2001, the same group that uncovered CO_2-V obtained two new phases, CO_2-II and CO_2-IV,[17,18] by heating the CO_2-III phase. CO_2-IV was first obtained by laser heating up to temperatures between 1000 and 1500 K in the pressure interval (12–30) GPa but it was also crystalized later[20] by external heating up to lower temperatures (750 K); lower temperature was needed to uncover CO_2-II (500 K) at 19 GPa.[18] Crystallographic analysis showed that CO_2-II can be described by the space groups $P4_2/mnm$ or $Pnnm$[19] whereas CO_2-IV fit well to both the tetragonal $P4_12_12$ or the pseudo-tetragonal *Pbcn*;[20] in both cases, molecules lose their molecular character being or strongly bent (the O-C-O angle measured was of 160° for CO_2-IV) or with clear dimerization signatures. These results pointed toward a scenario in that the transition between the molecular phase CO_2-I and the extended and non-molecular CO_2-V phase is performed through intermediate stable phases, CO_2-IV and CO_2-II, where the molecular character of carbon dioxide is lost gradually. This picture was strongly contested by Bonev *et al.*[21] by using quantum mechanical MP2 calculations. Starting from the crystalline structures defined previously, they found that the structures always converged to a molecular solid with intramolecular angles and distances typical of the molecular CO_2-I phase. In addition, they claimed that the available experimental results can be described using molecular solids with the crystalline structure $P4_2/mnm$ for CO_2-II and an orthorombic distorted phase for CO_2-IV. After that, Gorelli *et al.*[22] confirmed the molecular character of CO_2-II using new measurements of the Raman spectra of this solid phase, whereas Datchi *et al.*[32] obtained a new crystallographic description of the CO_2-IV phase as a rhombohedral $R\bar{3}c$. All these findings suggested that the intermediate scenario should not be correct and the extended covalent CO_2-V phase is produced by abrupt chemical reactions at very high temperature and pressure. Nowadays, the $P4_2/mnm$ for CO_2-II and the $R\bar{3}c$ for CO_2-IV can be considered the correct crystallographic structures. Figures 1(b) and 1(d) show the unit cells for both phases, and Fig. 2 shows the stability regions in the p–T plane. In these dates, in parallel, two new non-molecular phases were uncovered by strong compression of CO_2-III and CO_2-II at intermediate temperatures, the CO_2-VI phase[25] and the amorphous CO_2,[26] respectively, whose stability domain is shown in Fig. 2.

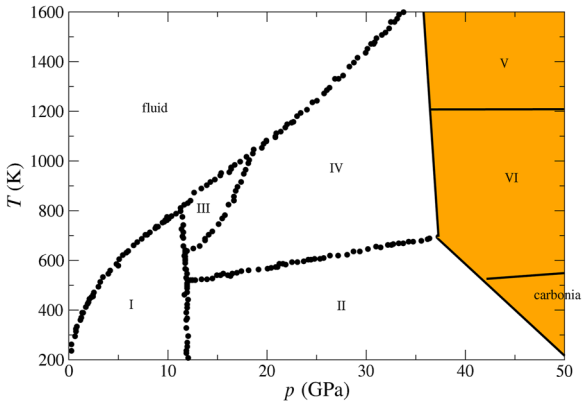

FIG. 2. Experimental phase diagram of carbon dioxide adapted with permission from Cogollo-Olivo *et al.*, Phys. Rev. Lett. **124**, 095701 (2020). Copyrighted by the American Physical Society. The non-molecular and amorphous phases are in the orange shaded area.

As commented above, the isothermal compression at ambient temperature of the CO_2-I phase produces the CO_2-III phase. This martensitic transition occurs sluggishly without a total conversion of the CO_2-I phase in the (12–20) GPa interval.[17] It is necessary to increase the temperature up to 400 K in order to eliminate any presence of the initial solid phase.[18] As previously commented, by heating CO_2-III, it was possible to transit to solid phases of higher temperature, however, the CO_2-III phase was not recovered

25 August 2025 09:47:05

Published under an exclusive license by AIP Publishing

in the inverse process (so, the transition was not found reversible). These experimental results carried out to conclude that this phase is metaestable in the region where it was discovered.[18] In 1993, Aoki *et al.*[10] determined experimentally the crystallographic structure for the CO_2-III phase as orthorombic *Cmca* with a < b lattice constants in complete agreement with (and probably strongly influenced by) that previously reported by Kutcha and Ethers[8] in 1989. A few years later, in 2007, Giordano and Datchi[29] uncover a new carbon dioxide phase, CO_2-VII at 20 GPa and at temperatures around 650 K, which presented the same space group as the CO_2-III phase but with a > b in agreement with the *Cmca* phase proposed by Bonev *et al.*[21] Thus, the idea of CO_2-III and CO_2-VII phases being the same phase grew rapidly. This aspect was, however, not completely settled till very recently[43] where the available experimental diffraction data were checked using *ab initio* calculations of the two different structures. They found that the *Cmca* structure proposed by Aoki *et al.*[10] was not compatible with the experimental data and these can be only described with the structure proposed for the CO_2-VII phase. In addition, their calculations starting with the experimental CO_2-III structure always converged to that of the CO_2-VII phase. Thus, they finally conclude that both phases are the same. The unit cell of this phase and its stability domain are given in Figs. 1 and 2.

There is no doubt that quantum mechanical calculations have been crucial in the determination of phase diagram of Fig. 2. The selection of this method is unquestionable since it allows studying both molecular and non-molecular structures without any *a priori* constraint. However, once the phase diagram region has been established where only molecular phases appear, it seems reasonable to study how classical molecular intermolecular potentials work for reproducing the molecular phase diagram of carbon dioxide. Moreover, the phase diagram prediction is a severe test for analyzing the accuracy of an intermolecular potential and it can be used for improving the model parameters choice as it was shown in the elaboration of TIP4P/2005 model for water[53] or the OPLS/2016 model[54] for methanol.

In a previous work,[39] we explored the ability of several potentials to predict the fluid-CO_2-I transition obtaining that the TraPPE model[55] provided the best results. We also concluded that the accuracy of this model resided in its high quadrupolar moment, which plays a major role for the stabilization of phase CO_2-I. In this work, we analyzed how the TraPPE intermolecular potential is able to predict the whole molecular phase diagram of carbon dioxide. As it will be shown, the shape of the predicted phase diagram is not very different, in qualitative terms, from that obtained experimentally. However, there are important differences in quantitative terms related with the size of the stability regions of phases CO_2-II, CO_2-III, and CO_2-IV and with the pressure where they start to be stable. These points and the model underestimation of the solid densities at high pressure must be taken into account in future model improvements.

II. MODELS AND SIMULATION DETAILS

A variety of models have been proposed for molecular simulation of carbon dioxide.[55–61] In this work, CO_2 was described with the TraPPE model.[55] In this model, CO_2 is a rigid linear molecule with the carbon atom C at the center of the molecule and oxygens atoms O placed to each carbon side and separated 1.16 Å from C. Each atom contains an interaction site consisting of a Lennard-Jones center and a partial charge with LJ parameters, ε_C/k_B = 27.0 K, ε_O/k_B = 79 K, σ_C = 2.8 Å, and σ_O = 3.05 Å, and charges q_C = 0.7 e and q_O = −0.35 e and Lorentz–Berthelot combining rules for the cross C–O interactions. The quadrupolar moment of the molecule is of 3.78 D Å. The model parameters were obtained by fitting to vapor–liquid equilibrium (VLE) data of the CO_2 and propane mixture. Thus, this model provides an accurate representation of the VLE of pure carbon dioxide. This feature is not exclusive of this model and other CO_2 descriptions achieve the same goal. As it has been shown in a previous work,[39] an appropriate description of the VLE data is reached with a reliable balance between dispersive and quadrupolar interactions. As a general rule, models with low dispersive interactions can predict properly the VLE data with enough high quadrupolar moment. The prediction of the solid–liquid equilibrium (SLE) does not follow the same rules. Solid *Pa*3 carbon dioxide, CO_2-I, is an fcc cubic crystal of the *Pa*3 space group (also denoted as αN_2) with *T*-like relative orientation between first neighbors. The stability of this structure in linear molecules is guaranteed by quadrupole–quadrupole interactions, i.e., the larger the quadrupole, the more stable the solid is. Since the fluid phase is by far less affected by the quadrupole (molecules have more rotation facility), the role of the quadrupole seems to be crucial in SLE prediction. In our previous work,[39] we have shown that models with similar prediction of the VLE data provided very different results of the melting point of carbon dioxide. As expected, we found that when quadrupole rises, the melting point also increases. Among the models studied, the TraPPE model has the highest quadrupole moment and it predicts the fluid-I coexistence line very accurately. It will be interesting to show how this model works for high pressure CO_2 solids where quadrupole–quadrupole interactions compete with compactness.

The methodology for determining the phase diagram of a pure substance has been described elsewhere.[62–65] Here, we will give only a brief guide of the procedure used and we refer the readers to these previous contributions for further details. The phase diagram determination starts by the calculation of initial coexistence thermodynamic states between the fluid phase and the different solid phases. These points were estimated here using two different methods. In the direct coexistence (DC) method,[65,66] a starting simulation box is constructed putting in contact both phases (fluid and solid phase); *NpT* simulations are performed at fixed pressure, *p*, and at different temperatures, *T*, in order to monitor if the system freezes (at temperatures below the melting temperature T_m) or melts (at temperatures above T_m); T_m at the working pressure, *p*, is estimated as the average between the lowest and highest temperature at which the system melts and freezes, respectively. Alternatively, the initial coexistence points were estimated by equating the chemical potentials of both phases. To this end, the chemical potential of both phases is evaluated as a function of *T* and *p* from the thermodynamic integration (TI) method.[67,68] This procedure requires the knowledge for both phases of the equation of state (EOS) and accurate values of the chemical potential in a reference thermodynamics state. As for the fluid phase, the chemical potential was accurately evaluated in the reference state using the Widom test particle insertion (TPI) method.[69] As for the solid phases, the chemical potential was computed at the reference state, using the Einstein molecule[70] (EM) method. Once the initial coexistence points are known, the Gibbs–Duhem (GD) integration method[71,72] is used for

25 August 2025 09:47:05

Published under an exclusive license by AIP Publishing

determining the fluid–solid coexistence lines for the different solid phases. This method consists basically of the Clausius–Clapeyron equation integration, which is performed involving exclusively independent simulations of both phases along the coexistence line. The crossing points between two different fluid–solid coexistence lines are triple points where the fluid and both solid phases coexist. These points are also considered as starting states in the GD method to draw the solid–solid coexistence lines. In the same way, the crossing points between two solid–solid lines with a common solid are used for obtaining additional solid–solid lines. The coexistence lines can be used to determine the regions of the thermodynamics state space where each phase stable. Thus, the boundary of the stability region of a X-phase is composed by the coexistence lines of the X-phase closest to a specific thermodynamic state where the X-phase is stable. It is normal to start this process by the fluid phase, which is the stable phase at enough low pressure and high temperature, and to continue with the stable phases in contact with the fluid phase. Once all the phases were analyzed in this way, the global phase diagram is completely drawn.

Simulations were carried out in the *NpT* and *NVT* ensembles. The anisotropic version of *NpT* simulations[67,68] was used for solid phases, whereas isotropic *NpT* was the option for the fluid phase. Anisotropic simulations are absolutely required for solid simulations in order to have the system free of stress. Simulations were performed using both Monte Carlo (MC) and molecular dynamics (MD) techniques.

MC simulations were performed in the EOS calculations and in the free energy determination at the reference states for both the fluid (using the TPI method) and the solid phases (with the EM method). They were organized in cycles of N movements with one change of volume per cycle (only in *NpT* simulations), and the rest of movements being translations and rotations with equal probability. The maximum volume, translation, and rotation moves were set in order to have 1/3 of accepted movements. Lennard-Jones (LJ) interactions were computed explicitly up to an atomic cutoff radius whereas the LJ contributions beyond this radius were evaluated including standard long range corrections. The Ewald (EW) summation method[68] was selected in most of the MC simulations for dealing with Coulombic interactions using the same cutoff radius for the real space contribution. The reaction field (RF) method was also used, as a complementary option, in the calculation of the chemical potential of the fluid phase using the TPI method. In this case, a molecular cutoff was considered.

Molecular dynamics (MD) were used in the DC, GD, and TPI methods. Equations of motion were integrated with the verlet leap-frog algorithm using a time constant of 1 fs. The velocity rescale thermostat[73] and the Parrinello–Rahman barostat[74] were used to keep constant temperature and pressure, respectively. Time constants were set to 1.97 and 2.12 ps, respectively, to avoid resonances, whereas compressibility was set to 5×10^{-7} bar. LJ interactions were dealt with in the same way as in MC-EW simulations. The particle mesh Ewald (PME) method[75] was chosen for dealing with Coulombic interactions using the same atomic cutoff radius as in MC-EW simulations.

The initial configurations for solid phases were constructed according to their crystallographic structure obtained experimentally. They were taken from the works of Aoki *et al.*[10] for CO_2-I, Datchi *et al.*[40] for CO_2-II, Giordano and Datchi[29] for CO_2-III, and Datchi *et al.*[32] for CO_2-IV. Once the coordinates of the carbon dioxide molecules in the unit cell are obtained, it is replicated in each spatial direction in order to have similar lengths in each axis. Initial fluid phase configuration was obtained by heating the CO_2-I solid phase at 2000 K under *NVT* simulations. The simulation box for the coexistence direct method was constructed using a solid and a fluid phase configuration equilibrated at a thermodynamic state close to the coexistence point. Both phases were put in contact with a small separation between them (around 0.15 nm). This configuration is first used in a very short *NVT* simulation (0.1 ns) at a temperature close to melting in which only the fluid phase is free to move. The final configuration of the previous step was used as the starting box for the *NpT* simulations considered in the coexistence direct method. In Table S1 of the supplementary material, the details of initial configuration boxes used in this work are given for the four solids, for the fluid, and for DC simulations, as well as the type of simulations performed with each box, the cutoff radius, and the accumulation period used in each case.

III. RESULTS AND DISCUSSION

The densities of the carbon dioxide solid phases obtained from simulations at 300 K are compared to experimental data shown in Fig. 3. Experimental data were taken from Liu[6] (CO_2-I), Datchi *et al.*[40] (CO_2-II), Yoo *et al.*[19] (CO_2-III), and Park *et al.*[20] (CO_2-IV). In the first three cases, the suggested Birch–Munaghan parameterization was used, whereas in the latter, a polynomial fit to the experimental data of Ref. 20 was considered. As can be seen, the model accurately predicts the density of CO_2-I at low pressure but it underestimates the experimental values at high pressures (from 3 GPa). The underestimation also holds for the II, III, and IV phases. The origin of this discrepancy could be attributed to the strong LJ repulsive part, which impedes the compressibility of the fluid.

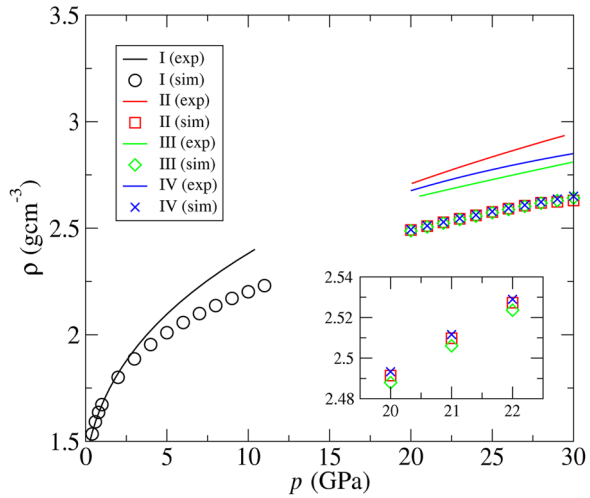

FIG. 3. Density ρ of the carbon dioxide solid phases as a function of pressure p at 300 K. The points indicate simulation data, and the full lines indicate experimental data (CO_2-I,[6] CO_2-II,[40] CO_2-III,[19] and CO_2-IV[20]).

25 August 2025 09:47:05

Published under an exclusive license by AIP Publishing

Probably, the substitution of the LJ repulsive part by the exponential-type term as that of the Buckingham function would improve the results. In addition, the TraPPE model is unable to provide significant differences between the densities of these phases as it appears in experiments. The model correctly predicts the lower density of III-phase with respect to II and IV phases; however, it erroneously gives the II-phase density smaller than that of IV-phase.

The excess chemical potential of fluid carbon dioxide was determined at the reference state, 800 K and 0.1 GPa. We used the TPI method in our MC-EW code. The μ^{ex} value was estimated using a system of $N = 576$ and three different cutoff radius (9.5, 12, and 15 Å) inserting in both cases 100 000 test particles with random position and orientation. Figure 4 shows the running μ^{ex} plotted as a function of the number of configurations used the calculation. As it can be seen, there is a slight dependence with the cutoff radius converging the μ^{ex}/k_BT value to 0.604 for cutoff radius higher than 12 Å. In order to be confident with this number, the μ^{ex} value was determined using two quicker tools than our MC-EW code also using the TPI method. In the first one, we used a home-made MC-RF code that makes use of the cutoff radius applied over a reference point in the molecule instead of that for each interaction site like in our MC-EW code. In the second one, MD-PME simulations with GROMACS 4.6.7 were performed for obtaining the trajectories that were re-analyzed through the TPI option in GROMACS. The results for both methods were in complete agreement with the previous results. For system sizes of $N = 576$ or greater (we used in this case, $N = 256$, 576, and 2048) and an enough cutoff radius, both tools provided the value 0.604(1). Thus, the chemical potential of the fluid phase as a function of T and p was determined using the thermodynamic integration method from this reference point.

The Helmholtz free energies A_{EM} of the different CO_2 solids were computed using the Einstein molecule method at the thermodynamic state $p = 7$ GPa and $T = 100$ K. In order to evaluate the finite size effect, calculations were performed for different number of molecules for each solid. The results, plotted in Fig. 5, indicate that A_{EM} raises slightly with the system size. We considered the Y-axis intercept of the linear fit of A_{EM} vs $1/N$ as the A_{EM} value in the thermodynamic limit. These values were used in the thermodynamic integration method in order to determine the chemical potential of the solid phases as a function of T and p. In order to show the accuracy of the thermodynamic integration method, free energies

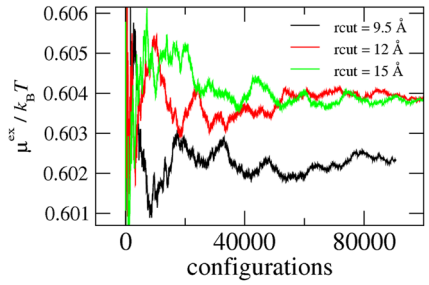

FIG. 4. Running excess chemical potential μ^{ex}/k_BT of CO_2 at 800 K and 0.1 GPa plotted as a function of the number of configurations used in the Widom particle insertion method for a system size of $N = 576$. Different curves correspond to different cutoff radius. Standard LJ long range corrections were included in the calculation.

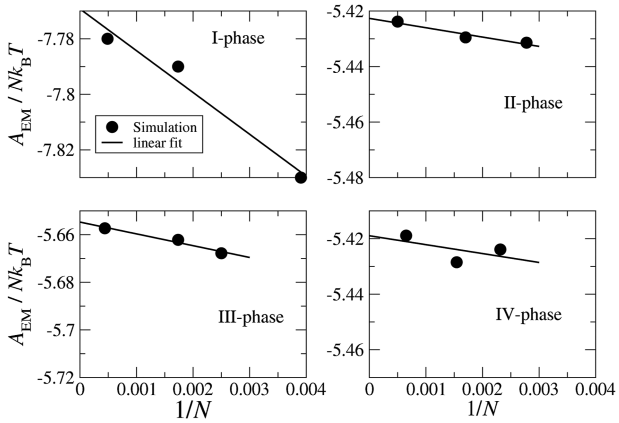

FIG. 5. Helmholtz free energy A_{EM} of the solids of this work obtained from the Einstein molecule method at 7 GPa and 100 K plotted as a function of the inverse of the number of carbon dioxide molecules. The points represent simulation data, and the full line represents a linear fit.

were computed at a different thermodynamic state from the reference one for comparison. The latter values were obtained using an intermediate size system for each phase and incorporating the finite size effects following the linear fits of Fig. 5. The results given in Table I indicated that deviations are less than 0.01 for most of the phases except for CO_2-IV. At low pressures, the agreement between both techniques for CO_2-I is excellent, and consequently, there will be no difference in the melting temperature estimation under these

TABLE I. Helmholtz free energy (in Nk_BT units) A_{EM} at temperature T, pressure p, and number of molecules N for the solid phases I, II, III, and IV obtained using the Einstein molecule method. In parenthesis, the free energy values obtained from the thermodynamic integration method using 7 GPa and 100 K as reference point are given.

		A_{EM}		
Phase	N	7 GPa–100 K	7 GPa–500 K	1 GPa–100 K
I	256	−7.831		−23.799
	576	−7.792		−23.767
	2048	−7.781		−23.760
	∞	−7.771	3.257 (3.251)	−23.751 (−23.751)
II	360	−5.431		
	588	−5.429		
	2000	−5.424		
	∞	−5.423	3.810 (3.803)	
III	400	−5.668		
	576	−5.662		
	2268	−5.657		
	∞	−5.655	3.680 (3.671)	
IV	432	−5.424		
	648	−5.428		
	1536	−5.419		
	∞	−5.419	3.749 (3.732)	

25 August 2025 09:47:05

Published under an exclusive license by AIP Publishing

conditions. However, this will not be the case for results at 7 GPa (especially for CO_2-IV). Thus, in order to raise the accuracy of melting temperature calculation at 7 GPa, we preferred to use in this case the reference state, 7 GPa and 500 K, for all the solid phases, which is closer to the melting temperature.

Once the chemical potential is known for fluid phase and the different solids, one can compare their values in order to identify at given T and p the more stable phase (that with lower chemical potential) or thermodynamic states where two or more phases coexist (those phases with equal chemical potential). In Fig. 6, the chemical potential of the fluid phase and solid CO_2-I are plotted as a function of T for the isobars 0.004, 1, and 7 GPa. In all the three cases, at low T, the stable phase is CO_2-I and at high T is the fluid phase with both regions separated by the coexistence temperature whose values are given in Table II. The coexistence temperature was estimated as that where the fit of the difference between chemical potentials as a function of temperature is null [as shown in Fig. 6(d)]. Note that the difference between chemical potentials substantially reduces as pressure increases. This point is at the origin of the greater sensibility of the melting temperature calculation at 7 GPa with respect to that at the lowest pressures. The difference between the fluid phase chemical potential and those of phases CO_2-II, III, and IV are presented in Fig. 7 for the isobar 7 GPa. As in the CO_2-I case, the differences between the chemical potential of both phases are also small. The melting temperatures at 7 GPa for these phases are also given in Table II.

Coexistence points between the fluid phase and the solid phases were also estimated using the direct coexistence method. In this methodology, NpT runs are perfomed using a starting simulation box that contains two phases. If temperature is lower than T_m, the liquid phase will freeze and the potential energy will decrease. If, however, the temperature is higher than T_m, the solid phase will melt and the potential energy will increase. We performed NpT simulations at several temperatures below and above the melting with a gap, in most cases, of 1 K. Figure 8 shows potential energy results for a system composed by the fluid and CO_2-I phase at the 0.004 and 7 GPa isobars. As can be seen, at 0.004 GPa for T< = 212 K, the system freezes and for T> = 213 K, the system melts. Thus, the

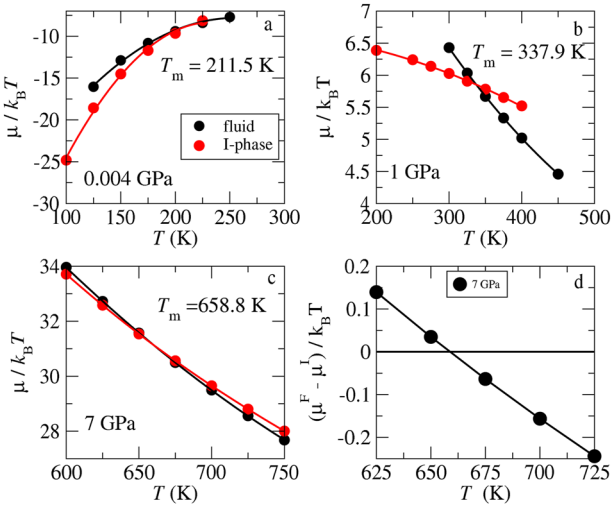

FIG. 6. Chemical potential μ of the fluid and the CO_2-I solid phase plotted as a function of temperature T at pressure (a) 0.004 GPa, (b) 1 GPa, and (c) 7 GPa. (d) Difference between the chemical potential of the fluid phase, μ^F, and that of the CO_2-I solid phase, μ^I, plotted as a function of T at 7 GPa.

TABLE II. Coexistence temperature T and pressure p obtained from the free energy calculations, the direct coexistence method, or by the Gibbs–Duhem integration. Uncertainty was estimated in 3 K for the direct coexistence method and 3 and 4 K for free energy calculations for low and high pressure, respectively. The last five rows are triple points determined from the crossing of two coexistence lines obtained from the Gibbs–Duhem integration.

p (GPa)	T (K)	Phases in equilibrium	Method
0.004	211.5	Fluid-I	Free energies
0.004	212.5	Fluid-I	Direct coexistence
0.020	214.6	Fluid-I	Free energies
0.020	215.5	Fluid-I	Direct coexistence
0.200	244.3	Fluid-I	Free energies
0.200	247.0	Fluid-I	Direct coexistence
1	337.9	Fluid-I	Free energies
1	339.5	Fluid-I	Direct coexistence
7	658.8	Fluid-I	Free energies
7	661.0	Fluid-I	Direct coexistence
7	668.1	Fluid-II	Free energies
7	665.5	Fluid-II	Direct coexistence
7	690.4	Fluid-III	Free energies
7	688.0	Fluid-III	Direct coexistence
7	692.4	Fluid-IV	Free energies
7	692.0	Fluid-IV	Direct coexistence
6.710	650.5	Fluid-I–II	Gibbs–Duhem
5.016	583	Fluid-I–III	Gibbs–Duhem
5.103	586.75	Fluid-I–IV	Gibbs–Duhem
5.490	609.1	Fluid-IV–III	Gibbs–Duhem
4.180	35	I–II–IV	Gibbs–Duhem

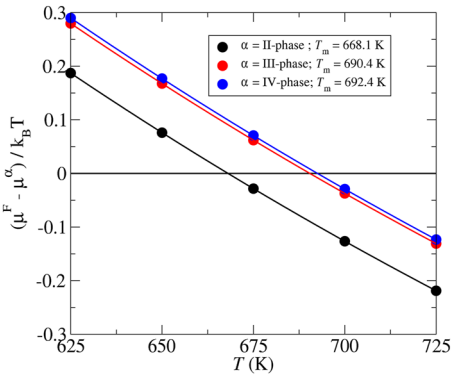

FIG. 7. Difference between the chemical potential of the fluid, μ^F, and that of the α phase, μ^α (with α = CO_2-II, CO_2-III, and CO_2-IV), plotted as a function of temperature T at 7 GPa. The points represent simulation data, and the full line represents fitting quadratic polynomials.

25 August 2025 09:47:05

Published under an exclusive license by AIP Publishing

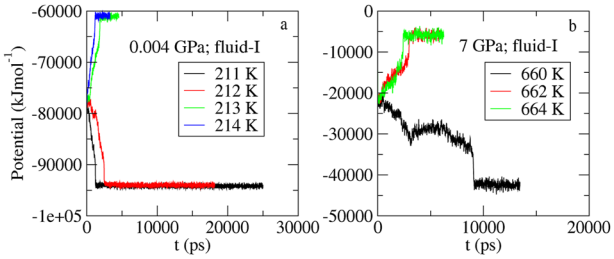

FIG. 8. Potential energy (in kJ per mole of simulation boxes) plotted as a function of time t for NpT runs of a two phases system containing carbon dioxide fluid and the CO_2-I solid phase at (a) 0.004 GPa and (b) 7 GPa.

melting temperature can be estimated to be 212.5 K. A similar analysis at 7 GPa leads us to determine T_m = 661 K. These values and those for other isobars and the corresponding for the rest of solids are given in Table II. As it can be seen, there is a great agreement between both routes according to the estimated uncertainty for both techniques.

We considered the direct coexistence T_m results as the starting thermodynamic states in the GD method in order to obtain the coexistence lines between the fluid and the different solid phases. We will now use these lines to identify the stability region of the fluid phase as well as the solid phases that coexist with it as follows. At given T^*, the lowest coexistence (or melting) pressure with the fluid will define the upper bound of the pressure interval where the fluid is the thermodynamically stable phase. The corresponding solid will be the stable phase that coexists with the fluid at T^*. By repeating this analysis at different T^*, the stability region of the fluid phase and the solid phases that coexist with it will be defined. When the melting pressure at a specific T^* is equal for two solids, this state will correspond with a triple point where both solid phases coexist with the fluid. In Fig. 9(a), the pressure of the fluid-CO_2-I coexistence line, $p_{F\text{-}I}$, minus those corresponding to the different fluid–solid lines, $p_{F-\alpha}$, are plotted as a function of temperature. Following previous comments, in this graph, at given temperature, $p_{F\text{-}I}-p_{F\text{-}\alpha} < 0$ indicates lower melting pressure of I phase with respect to the α phase; $p_{F\text{-}I}-p_{F\text{-}\alpha} < p_{F\text{-}I}-p_{F-\beta}$ reflects lower melting pressure of the β phase than that of the α solid; and triple points are those where "<" changes to "=" in previous relations. Thus, triple points are located at 583, 586.75, 609.1, and 650.5 K (the corresponding p-T states are given in Table II and are highlighted in Fig. 9). The temperature of the triple point fluid-CO_2-IV-CO_2-III is better observed in Fig. 9(b), where the pressure difference between the fluid-CO_2-IV and the fluid-CO_2-III lines is shown. These values divide the temperature range in different intervals according to the stable solid phase in contact with the fluid: the stable phase for T < 583 K is CO_2-I, between 583 and 609.1 K is CO_2-III, and for T > 609.1 K is CO_2-IV. Thus, the region of the fluid phase where it is thermodynamically stable is bounded by the fluid-I coexistence line below 583 K, by the fluid-III line between 583 and 609.1 K, and by the fluid-IV line for T > 609.1 K.

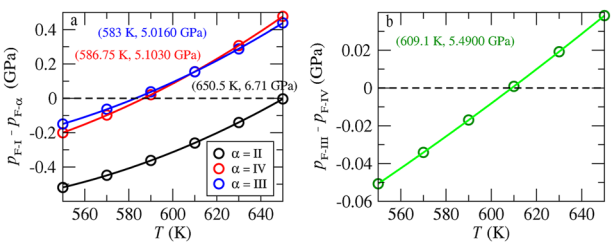

FIG. 9. (a) Difference between the coexistence pressure fluid-I, $p_{F\text{-}I}$, and that of the fluid-α, $p_{F\text{-}\alpha}$ plotted as a function of temperature T with α = II, III, and IV solid phases. (b) Difference $p_{F\text{-}III}-p_{F\text{-}IV}$. Pressure p and temperature T of the triple points are highlighted in the figure.

Solid–solid coexistence lines were determined from the GD method using the triple points recently obtained as starting points. The corresponding p-T values are shown in Fig. 10. This figure also includes the fluid–solid coexistence line recently described. First, it is worth noting that the I–III line and the IV–III line could be determined only for temperatures higher than 175 K. Below this temperatur,e III phase transforms in a different phase which is unstable with respect to I phase (as it will be shown in the following). Moreover, the I–II line crosses the I–IV line at 35 K. This new triple point was also used to determine the IV–II coexistence line from this point, which is also plotted in Fig. 10.

Now, we use results of Fig. 10 to explore the stability region of the CO_2-I phase. As shown recently, the CO_2-I phase is stable immediately below the fluid-I line for temperatures lower than 583 K. Thus, comparing the coexistence pressure given by the I-α lines at each T^* in this region, one can conclude that above 175 K, the III phase is the most stable solid in contact with I-phase, between 175 and 35 K this is the IV phase, and below 35 K it is the II phase; their corresponding coexistence lines together with the fluid-I line define the stability region of I-phase. To continue, the boundary of the stability region of the III solid is analyzed. As previously shown, the I–III line bounds this region for low pressures and the fluid-III for high temperatures. The high pressure boundary is defined by the III–IV coexistence line. Note that it is not necessary to know the II–III coexistence line since IV–II line indicates that for pressures higher than those of the I–III line, the IV phase is more stable than the II phase. The last two phases to be studied are the IV and II phases. The stability region for IV-phase is bounded by the

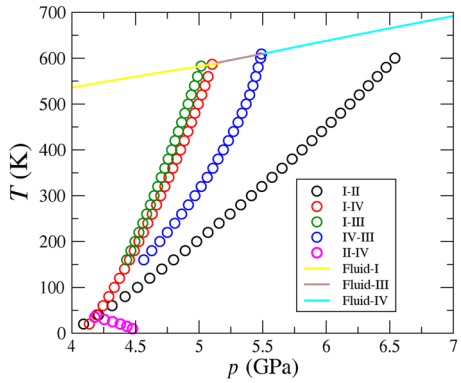

FIG. 10. Solid–solid and solid–fluid coexistence lines in the pressure–temperature, p–T, plane.

25 August 2025 09:47:05

Published under an exclusive license by AIP Publishing

fluid-IV, III–IV, I–IV, and IV–II lines. As for the II-phase, it occupies a small region defined by I–II and II–IV lines.

According to this analysis, the global phase diagram is that plotted in Fig. 11. As was exposed, at low pressures, the stable phase is the I-phase, whereas at high pressures, it is the IV solid phase. In between both regions, there appear two small islands where the III-phase and the II phase are the more stable phases. In the first case, this region comprises temperatures above 175 K, and for the second case, it comprises temperatures below 35 K. As in experiments (see Fig. 2), the model predicts the existence of stability regions for all the phases as well as their relative location. However, the size and the exact location in the phase diagram are not quantitatively predicted. This is better observed in Fig. 12 where the TraPPE phase diagram is compared to the experimental one. Here, it is clear that the I-IV phase is predicted at significantly low pressures and the stability regions of III and II phases are significantly smaller. The best quantitative prediction is the fluid-I coexistence line as it is shown in Fig. 13. The fluid-IV coexistence line, also compared to experimental data in this figure, is overestimated by ~30 K at the lowest pressures and this discrepancy increases with pressure. It is also worth noting that according to the classical statistical mechanics,[76] the p-T slopes of coexistence lines at 0 K are finite (see I–II and II–IV coexistence lines of the TraPPE model in Figs. 11 and 12). This is, however, not expected experimentally since following the third law of thermodynamics, the entropy variation between perfect ordered solid phases at 0 K is null[76] and then $dp/dT = \Delta S/\Delta V$ is zero (see I–II experimental line in Fig. 12, where $dp/dT = 0$).

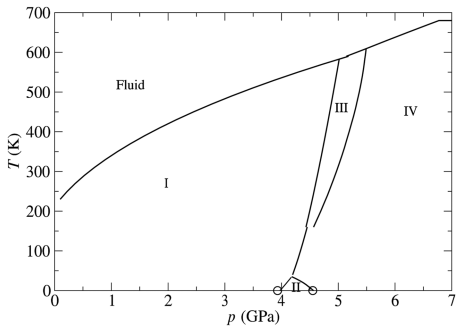

FIG. 11. Phase diagram of CO_2 by the TraPPE model.

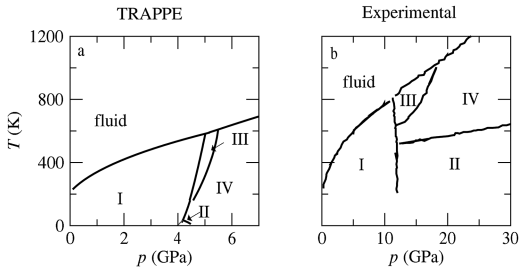

FIG. 12. Comparison of the phase diagram of CO_2 from the (a) TraPPE model and (b) experiments.[41,48]

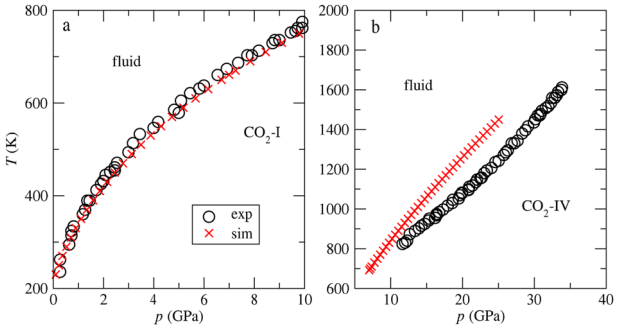

FIG. 13. (a) Fluid-I and (b) fluid-IV coexistence lines compared to experimental data.[41,48]

At 0 K, the Gibbs free energy coincides with the enthalpy since the TS term is null. The equal chemical potential criterion for determining coexistence points between phases transforms at 0 K into the equal enthalpy condition.[76] The determination of the enthalpy at 0 K can be easily estimated by extrapolating the enthalpy values obtained from consecutive NpT simulations at decreasing temperatures. Thus, this procedure allows alternatively determining the stability of the different solid phases at 0 K and it can be used as a strong thermodynamic consistency check of our results obtained previously. To this end, we have performed these NpT simulations for the I, II, and IV phases between 3 and 5 GPa with a 0.25 GPa step from 100 to 5 K. Extrapolated enthalpies at 0 K are compared in Fig. 14 by plotting the difference between the enthalpy of phases II and IV with respect to that of I-phase. As it can be seen, this method gives that the most stable phase is CO_2-I up to 3.93 GPa, CO_2-II between this pressure and 4.55 GPa, and CO_2-IV beyond 4.55 GPa. These coexistence pressures are plotted as empty points in Fig. 11 and it can be seen that it agrees very accurately with our previous predictions pointing toward the accuracy of our results.

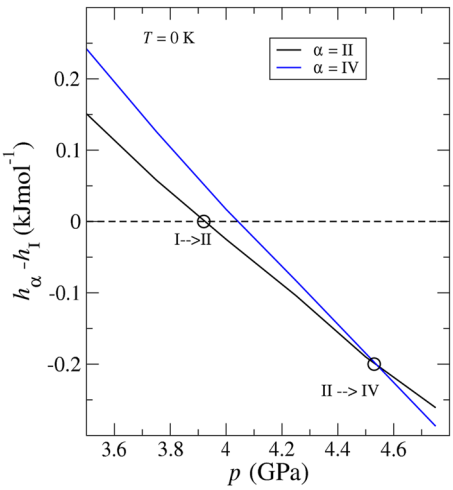

FIG. 14. Difference between enthalpy of the α phase (with α = II and IV), h_α, and that of the I-phase, h_I, at 0 K. Transitions between phases are highlighted by empty points.

25 August 2025 09:47:05

Published under an exclusive license by AIP Publishing

As exposed in Sec. I, the I-III transition is martensitic.[12] The III phase can be obtained experimentally by compressing I-phase up to 12 GPa at room temperature T and III-phase can be recovered from III-phase below 8–10 GPa.[18] We tried to emulate the I–> III transition in consecutive 4 ns NpT anisotropic simulations from 1 to 17 GPa with a 0.5 GPa step at 100 K. We found that at 16.5 GPa, the I-phase converts into a new phase. One can observe this transition by plotting the lattice constants as a function of pressure as shown in Fig. 15(a); at 16.5 GPa, the cubic unit cell (a = b = c) changes to an orthorombic cell with distinct a, b, and c values. We found these a, b, and c values correspond with those of the III-phase at this pressure. In addition, we compare the CC, OO, and CO rdf of the new phase and they coincide with those of the III phase at this state. This is shown for the CC rdf in Fig. 15(b), where, in addition, the CC rdf for the different solids at 17 GPa are shown in order to highlight the structural differences between phases. The III–> I transition was also studied with an equivalent procedure but starting with the III phase at 10 GPa and reducing pressure down to 0.2 GPa. The lattice constants are given in Fig. 16(a) as a function of pressure. As can be seen, the III phase converts into a new phase below 1 GPa. The a, b, and c lattice constants collapse in the same value as a = b = c, which coincides with the corresponding values of the I-phase. The CC, CO, and OO rdf of the new phase also coincide with the I-phase (not shown here) under the same conditions, confirming that the new phase is the I-phase.

It is also worth noting that III phase does not transit directly to I-phase; first, it converts into a new phase (termed here IIIb) below 5 GPa that persists down to 2 GPa. Long NpT simulation runs (up to 30 ns) of this new phase, under these thermodynamic conditions, showed no change in its crystalline structure, suggesting that IIIb is not an intermediate transient state between III and I phases but a new phase. In addition, we found that by isothermal compression of IIIb, it converts again in the III phase, i.e., the III-IIIb transition is reversible. From a structural point of view, the IIIb has significant differences with respect to the other phases (I, II, III, and IV), as shown in Fig. 16(b). To go deeper in this aspect, as shown in Fig. 1, the carbon dioxide molecules in the III phase forms a 37° angle with the z axis and they are in the plane YZ. In the new IIIb phase, the first angle remains equal; however, carbon dioxide molecules separate slightly (around 10°) from the YZ plane. A reanalysis of the

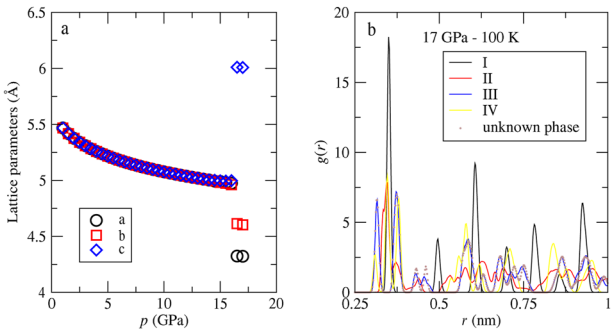

FIG. 15. I–III transition. (a) Lattice constants a, b, and c of the unit cell plotted as a function of pressure p at 100 K. (b) Radial distribution function between carbon atoms plotted as a function of distance r for the I, II, III, and IV solid phases and the unknown phase at 17 GPa.

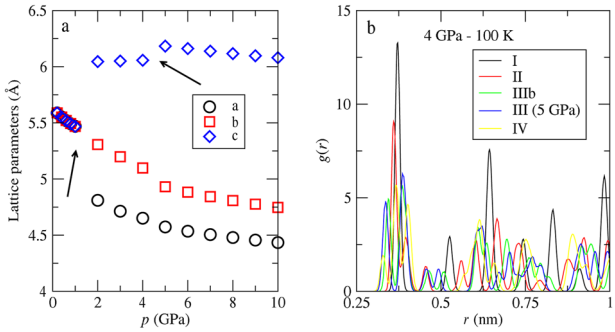

FIG. 16. III-I transition. (a) Lattice constants a, b, and c of the unit cell plotted as a function of pressure p at 100 K. (b) Radial distribution function between carbon atoms plotted as a function of distance r for the I, II, III, IIIb, and IV solid phases at 17 GPa.

enthalpies at OK including the IIIb phase showed that the more stable phase below 3.77 GPa is CO_2-I, between 3.77 and 4.34 GPa CO_2-IIIb, between 4.34 and 4.55 GPa CO_2-II, and beyond 4.55 GPa the CO_2-IV phase. Probably, at higher temperatures than 0 K, the IIIb phase will continue being the more stable phase in a similar interval than that at 0 K. However, this interval will reduce as T rises since free energy calculations above 100 K indicate that this phase is less stable than I-phase. To conclude, if we would have also considered this new phase (denoted here as IIIb) to compute the global phase diagram, it would steal a small piece of region to I and II phases below 100 K.

IV. CONCLUSIONS

In this work, the phase diagram of carbon dioxide is explored by Monte Carlo and molecular dynamics simulations of the TraPPE intermolecular potential in the region of the phase diagram where CO_2 is still a molecular solid in the experiments. Initial fluid–solid coexistence points were determined using both the direct coexistence method and by chemical potential evaluation of the involved phases. The chemical potential was determined from the thermodynamic integration method using as reference thermodynamic states 800 K and 0.1 GPa for the fluid phase, and 100 K and 7 GPa and 500 K and 7 GPa for the solids. In the former case, the chemical potential was estimated by the Widom test particle insertion method and in the latter by the Einstein molecule method. The initial coexistence points were used in the Gibbs–Duhem method to estimate the fluid–solid coexistence lines. Crossing points between these lines were also used as initial points for the GD determination of solid–solid lines. Once all the possible coexistence lines were determined, the global phase diagram was defined.

It was shown that the TraPPE model is able to accurately describe the density of CO_2-I phase up to 3 GPa, the fluid-CO_2-I transition up to 10 GPa (this was analyzed in a previous contribution but for pressures lower than 1 GPa), and to define stability regions for CO_2-I, CO_2-II, CO_2-III, and CO_2-IV, as well as the fluid phase. As in experiments, the CO_2-I phase is the low pressure solid phase, CO_2-IV the solid phase at high temperature and pressure, and CO_2-III appears in small island at the center of the phase diagram, respectively. However, the predicted stability region of CO_2-II

25 August 2025 09:47:05

Published under an exclusive license by AIP Publishing

and CO_2-III is very small, and the pressure at which CO_2-II, CO_2-III, and CO_2-IV become stable is significantly low. In addition, the density of solids is underestimated for pressures higher than 3 GPa. It seems that the model fails in the high pressure predictions. This deficiency also appears in water models; for instance, at 400 K, the TIP4P/2005 model[53] predicts the fluid–ice VII transition at 7 GPa, whereas in experiments, it appears at 2 GPa.[77] It is clear that there is room for improvement. Further work along these lines is required. A key point seems to be to improve the compressibility of the model at high pressures, keeping the correct quadrupolar–quadrupolar interactions, which are essential in the stability of solid phases, especially at low pressures. Compressibility could be improved by changing the repulsive part of the LJ potential by an exponential term or a MIE potential with $n < 12$, which raises more slowly than the LJ $(\sigma/r)^{12}$ as r is reduced. This point is, however, far to be simple. On the one hand, the change of the repulsive term will also imply changes in some of the other model parameters, making it a difficult task to properly fix the quadrupolar interaction (reducing the repulsion exponent will likely require an increase in charges to compensate, since the repulsion exponent tends to influence the vapor pressure in a way that is similar to partial charges, as shown by Pottof and Bernard-Brunel[78]). On the other hand, there are some evidence[79] that increasing the n term in the MIE potential (i.e., a steeper repulsive term) improves the results at high pressures. Thus, it will, probably, be necessary for a significantly more complex functional form to get all of the phase behavior correct. It seems interesting (despite that I, II, III, and IV phases are molecular without bending and similar intramolecular bond lengths) to explore how introducing molecular flexibility can help improve the phase diagram taking into account the extremely high pressures involved.

SUPPLEMENTARY MATERIAL

The supplementary material provides further details of our simulations; the pressure-temperature data of the coexistence lines of the phase diagram of the TraPPE model; the volume, potential energy, and configurational enthalpy of the different solid phases between 100 and 0 K and from 3 to 5 GPa; and the coexistence pressures obtained at 0 K from the equal enthalpy condition.

ACKNOWLEDGMENTS

The authors acknowledge the support from the Spanish Ministry of Science and Innovation under Grant Nos. PID2020-115722GB-C22, PID2021-125081NB-I00, PID2022- 136919NB-C31, PID2023-147148NB-I00, and PID2024-158030NB-I00. The authors acknowledge CESGA (Centro de Supercomputación de Galicia) for the use of their computation facilities.

AUTHOR DECLARATIONS

Conflict of Interest

The authors have no conflicts to disclose.

Author Contributions

D. González-Salgado: Conceptualization (equal); Data curation (equal); Formal analysis (equal); Funding acquisition (equal); Investigation (equal); Supervision (equal); Writing – original draft (equal); Writing – review & editing (equal). **M. M. Piñeiro**: Conceptualization (equal); Data curation (equal); Formal analysis (equal); Funding acquisition (equal); Investigation (equal); Supervision (equal); Writing – original draft (equal); Writing – review & editing (equal). **C. Vega**: Conceptualization (equal); Data curation (equal); Formal analysis (equal); Funding acquisition (equal); Investigation (equal); Supervision (equal); Writing – original draft (equal); Writing – review & editing (equal).

DATA AVAILABILITY

The data that support the findings of this study are available within the article and its supplementary material.

REFERENCES

[1] N. MacDowell, N. Florin, A. Buchard, J. Hallett, A. Galindo, G. Jackson, C. S. Adjiman, C. K. Williams, N. Shah, and P. Fennell, Energy Environ. Sci. **3**, 1645 (2010).
[2] P. W. Bridgman, Phys. Rev. **3**, 153 (1914).
[3] A. Simon and K. Peters, Acta Crystallogr., Sect. B **36**, 2750 (1980).
[4] R. C. Hanson and L. H. Jones, J. Chem. Phys. **75**, 1102 (1981).
[5] B. Olinger, J. Chem. Phys. **77**, 6255 (1982).
[6] L.-g. Liu, Earth Planet. Sci. Lett. **71**, 104 (1984).
[7] R. C. Hanson, J. Phys. Chem. **89**, 4499 (1985).
[8] B. Kuchta and R. D. Etters, Phys. Rev. B **38**, 6265 (1988).
[9] K. Aoki, H. Yamawaki, and M. Sakashita, Phys. Rev. B **48**, 9231 (1993).
[10] K. Aoki, H. Yamawaki, M. Sakashota, Y. Gotoh, and K. Takemura, Science **263**, 356 (1994).
[11] H. Olijnyk and A. P. Jephcoat, Phys. Rev. B **57**, 879 (1998).
[12] C. S. Yoo, H. Cynn, F. Gygi, G. Galli, V. Iota, M. Nicol, S. Carlson, D. Häusermann, and C. Mailhiot, Phys. Rev. Lett. **83**, 5527 (1999).
[13] S. Serra, C. Cavazzoni, G. L. Chiarotti, S. Scandolo, and E. Tosatti, Science **284**, 788 (1999).
[14] V. Iota, C. S. Yoo, and H. Cynn, Science **283**, 1510 (1999).
[15] B. Holm, R. Ahuja, A. Belonoshko, and B. Johansson, Phys. Rev. Lett. **85**, 1258 (2000).
[16] O. Tschauner, H.-k. Mao, and R. J. Hemley, Phys. Rev. Lett. **87**, 075701 (2001).
[17] C.-S. Yoo, V. Iota, and H. Cynn, Phys. Rev. Lett. **86**, 444 (2001).
[18] V. Iota and C.-S. Yoo, Phys. Rev. Lett. **86**, 5922 (2001).
[19] C. S. Yoo, H. Kohlmann, H. Cynn, M. F. Nicol, V. Iota, and T. LeBihan, Phys. Rev. B **65**, 104103 (2002).
[20] J.-H. Park, C. S. Yoo, V. Iota, H. Cynn, M. F. Nicol, and T. Le Bihan, Phys. Rev. B **68**, 014107 (2003).
[21] S. A. Bonev, F. Gygi, T. Ogitsu, and G. Galli, Phys. Rev. Lett. **91**, 065501 (2003).
[22] F. A. Gorelli, V. M. Giordano, P. R. Salvi, and R. Bini, Phys. Rev. Lett. **93**, 205503 (2004).
[23] M. Santoro, J.-f. Lin, H.-k. Mao, and R. J. Hemley, J. Chem. Phys. **121**(6), 2780 (2004).
[24] V. M. Giordano, F. Datchi, and A. Dewaele, J. Chem. Phys. **125**, 054504 (2006).
[25] V. Iota, C.-S. Yoo, J.-H. Klepeis, Z. Jenei, W. Evans, and H. Cynn, Nat. Mater. **6**(1), 34 (2006).
[26] M. Santoro, F. A. Gorelli, R. Bini, G. Ruocco, S. Scandolo, and W. A. Crichton, Nature **441**, 857 (2006).
[27] M. Santoro and F. A. Gorelli, Chem. Soc. Rev. **35**, 918–931 (2006).
[28] T. Kume, Y. Ohya, M. Nagata, S. Sasaki, and H. Shimizu, J. Appl. Phys. **102**, 053501 (2007).
[29] V. M. Giordano and F. Datchi, Europhys. Lett. **77**, 46002 (2007).
[30] J. A. Montoya, R. Rousseau, M. Santoro, F. Gorelli, and S. Scandolo, Phys. Rev. Lett. **100**, 163002 (2008).
[31] J. Sun, D. D. Klug, R. Martonák, J. A. Montoya, M.-S. Lee, S. Scandolo, and E. Tosatti, Proc. Natl. Acad. Sci. U. S. A. **106**, 6077 (2009).

25 August 2025 09:47:05

Published under an exclusive license by AIP Publishing

[32]F. Datchi, V. M. Giordano, P. Munsch, and A. M. Saitta, Phys. Rev. Lett. **103**, 185701 (2009).
[33]V. M. Giordano, F. Datchi, F. A. Gorelli, and R. Bini, J. Chem. Phys. **133**, 144501 (2010).
[34]A. Sengupta and C.-S. Yoo, Phys. Rev. B **82**, 012105 (2010).
[35]K. D. Litasov, A. F. Goncharov, and R. J. Hemley, Earth Planet. Sci. Lett. **309**, 318 (2011).
[36]B. Boates, S. Hamel, E. Schwegler, and S. A. Bonev, J. Chem. Phys. **134**, 064504 (2011).
[37]A. Sengupta, M. Kim, C.-S. Yoo, and J. S. Tse, J. Phys. Chem. C **116**, 2061–2067 (2012).
[38]M. Santoro, F. A. Gorelli, R. Bini, J. Haines, O. Cambon, C. Levelut, J. A. Montoya, and S. Scandolo, Proc. Natl. Acad. Sci. U. S. A. **109**, 5176 (2012).
[39]G. Pérez-Sánchez, D. González-Salgado, M. M. Piñeiro, and C. Vega, J. Chem. Phys. **138**, 084506 (2013).
[40]F. Datchi, B. Mallick, A. Salamat, G. Rousse, S. Ninet, G. Garbarino, P. Bouvier, and M. Mezouar, Phys. Rev. B **89**, 144101 (2014).
[41]F. Datchi, G. Weck, A. M. Saitta, Z. Raza, G. Garbarino, S. Ninet, D. K. Spaulding, J. A. Queyroux, and M. Mezouar, Phys. Rev. B **94**, 014201 (2016).
[42]I. Gimondi and M. Salvalaglio, J. Chem. Phys. **147**, 114502 (2017).
[43]W. Sontising, Y. N. Heit, J. McKinley, and G. J. O. Beran, Chem. Sci. **8**, 7374 (2017).
[44]Y. Han, J. Liu, L. Huang, and J. Li, npj Quantum Mater. **4**, 10 (2019).
[45]Y. Han, J. Liu, and J. Li, Int. J. Quantum Chem. **120**, e26397 (2020).
[46]L. Huang, Y. Han, X. He, and J. Li, RSC Adv. **10**, 236 (2020).
[47]H. Nabata, M. Takagi, K. Saita, and S. Maeda, RSC Adv. **10**, 22156 (2020).
[48]B. H. Cogollo-Olivo, S. Biswas, S. Scandolo, and J. A. Montoya, Phys. Rev. Lett. **124**, 095701 (2020).
[49]W.-G. Li, Y.-D. Gan, Z.-X. Bai, X.-H. Li, F.-S. Liu, Z.-T. Liu, Q.-J. Liu, D. Hong, and X.-H. Chang, Phys. Chem. Chem. Phys. **24**, 4462 (2022).
[50]D. Gambin, K. K. Dudek, M. R. Dudek, J. N. Grima, and R. Gatt, Phys. Status Solidi B **259**, 2200419 (2022).
[51]K. D. Litasov, V. V. Brazhkin, N. E. Sagatov, and T. M. Inerbaev, JETP Lett. **119**, 205 (2024).
[52]W. Duschek, R. Kleinrahm, and W. Wagner, J. Chem. Thermodyn. **22**, 841 (1990).
[53]J. L. F. Abascal and C. Vega, J. Chem. Phys. **123**, 234505 (2005).
[54]D. Gonzalez-Salgado and C. Vega, J. Chem. Phys. **145**, 034508 (2016).
[55]J. J. Potoff and J. I. Siepmann, AIChE J. **47**, 1676 (2001).
[56]C. S. Murthy, K. Singer, and I. R. McDonald, Mol. Phys. **44**, 135 (1981).
[57]J. G. Harris and K. H. Yung, J. Phys. Chem. **99**, 12021 (1995).
[58]Z. Zhang and Z. Duan, J. Chem. Phys. **122**, 214507 (2005).
[59]T. Merker, C. Engin, J. Vrabec, and H. Hasse, J. Chem. Phys. **132**, 234512 (2010).
[60]C. G. Aimoli, E. J. Maginn, and C. R. A. Abreu, J. Chem. Phys. **141**, 134101 (2014).
[61]H. R. Dittmar and P. G. Kusalik, J. Chem. Phys. **145**, 134504 (2016).
[62]C. Vega, E. Sanz, J. L. F. Abascal, and E. G. Noya, J. Phys. Condens. Matter **20**, 153101 (2008).
[63]D. G. Salgado and C. Vega, J. Chem. Phys. **132**, 094505 (2010).
[64]D. Gonzalez-Salgado, A. Dopazo-Paz, P. Gomez-Alvarez, J. M. Miguez, and C. Vega, J. Phys. Chem. B **115**, 3522 (2011).
[65]M. M. Conde, M. A. Gonzalez, J. L. F. Abascal, and C. Vega, J. Chem. Phys. **139**, 154505 (2013).
[66]J. Costandy, V. K. Michalis, I. N. Tsimpanogiannis, A. K. Stubos, and I. G. Economou, J. Chem. Phys. **143**, 094506 (2015).
[67]M. P. Allen and D. J. Tildesley, *Computer Simulation of Liquids* (Oxford University Press, 1987).
[68]D. Frenkel and B. Smit, *Understanding Molecular Simulation* (Academic Press, London, 2002).
[69]B. Widom, J. Chem. Phys. **39**, 2808 (1963).
[70]C. Vega and E. G. Noya, J. Chem. Phys. **127**, 154113 (2007).
[71]D. A. Kofke, J. Chem. Phys. **98**, 4149 (1993).
[72]D. A. Kofke, Mol. Phys. **78**, 1331 (1993).
[73]G. Bussi, D. Donadio, and M. Parrinello, J. Chem. Phys. **126**, 014101 (2007).
[74]M. Parrinello and A. Rahman, J. Appl. Phys. **52**, 7182 (1981).
[75]U. Essmann, L. Perera, M. L. Berkowitz, T. Darden, H. Lee, and L. G. Pedersen, J. Chem. Phys. **103**, 8577 (1995).
[76]J. L. Aragones, E. G. Noya, J. L. F. Abascal, and C. Vega, J. Chem. Phys. **127**, 154518 (2007).
[77]J. L. Aragones and C. Vega, J. Chem. Phys. **130**, 244504 (2009).
[78]J. J. Potoff and D. A. Bernard-Brunel, J. Phys. Chem. B **113**, 14725 (2009).
[79]R. A. Messerly, M. C. Anderson, S. M. Razavi, and J. R. Elliott, Fluid Phase Equilib. **483**, 101 (2019).

25 August 2025 09:47:05

Published under an exclusive license by AIP Publishing